

# Biophysical *Journal*

Volume 119

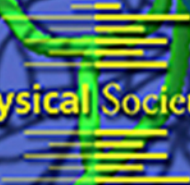
Number 1

July 7, 2020



[www.biophysj.org](http://www.biophysj.org)

The Premier Journal of Quantitative Biology



Biophysical Society



CellPress  
Partner Journal

## Uncovering the Secrets of the Keratin Cytoskeleton

Cells contain 3D scaffolds of interconnected filament systems referred to as the cytoskeleton. Three major filament systems encompassing actin-based microfilaments, microtubules and intermediate filaments contribute in different ways to the specific biomechanics of distinct cell types. Protecting the body from mechanical stress is a major task of surface-covering epithelial cells. The stress-protective function is in large part determined by keratin intermediate filaments forming networks with cell type-specific spatial arrangements. Intermediate filaments exhibit unique mechanical properties. They are semiflexible polymers with a persistence length of  $\sim 1 \mu\text{m}$  and are highly elastic with an extensibility up to 3.6-fold. They are also mechanosensitive, responding to increasing tension by strain-stiffening.

To understand how the unique 3D network arrangement of the keratin cytoskeleton affects cell mechanics, we are working to reconstruct the entire keratin filament system of single cells. To this end, fluorescent keratin reporters are used to label keratin filaments and high-resolution imaging is used to create digital representation of the network. The cover image for the July 7 issue of the *Biophysical Journal* shows the result for a single epithelial cell presenting an inside view of the keratin cytoskeleton. Fluorescence recordings that were obtained in 23 focal planes were subjected to image analysis for subsequent filament segmentation. The cover image does not provide information on filament brightness, (i.e., filament bundling) but classifies different filaments by color: red, apical filaments; yellow, lateral filaments; blue, perinuclear filaments; green, basal filaments.

The relationship between keratin filament organization and mechanical properties is key to explaining pathogenic mechanisms of keratin disorders, a group of hereditary epidermal diseases caused by single-point mutations of keratin-encoding genes and characterized by blisters. In addition, time-lapse imaging of living cells has uncovered an unexpected range of dynamic reorganization of the keratin system, which is essential for understanding wound healing and invasion of transformed malignant cells.

Our study in the current issue of the *Biophysical Journal* is based on recordings of keratin network dynamics in vital cells and proposes a model for bundling keratin intermediate filaments, taking interfilament electrostatic and hydrophobic interactions into account.

For further information visit our website at [www.moca.ukaachen.de](http://www.moca.ukaachen.de)

- Ehud Haimov, Reinhard Windoffer, Rudolf Leube, Michael Urbakh, Michael Kozlov

# Model for Bundling of Keratin Intermediate Filaments

Ehud Haimov,<sup>1</sup> Reinhard Windoffer,<sup>2</sup> Rudolf E. Leube,<sup>2</sup> Michael Urbakh,<sup>3,\*</sup> and Michael M. Kozlov<sup>4,\*</sup>

<sup>1</sup>School of Physics and Astronomy, Raymond and Beverly Sackler Faculty of Exact Sciences, Tel-Aviv University, Tel-Aviv, Israel; <sup>2</sup>Institute of Molecular and Cellular Anatomy, RWTH Aachen University, Aachen, Germany; <sup>3</sup>School of Chemistry, Raymond and Beverly Sackler Faculty of Exact Sciences and <sup>4</sup>Department of Physiology and Pharmacology, Sackler Faculty of Medicine, Tel-Aviv University, Tel-Aviv, Israel

**ABSTRACT** Keratin intermediate filaments form dynamic intracellular networks, which span the entire cytoplasm and provide mechanical strength to the cell. The mechanical resilience of the keratin intermediate filament network itself is determined by filament bundling. The bundling process can be reproduced in artificial conditions in the absence of any specific cross-linking proteins, which suggests that it is driven by generic physical forces acting between filaments. Here, we suggest a detailed model for bundling of keratin intermediate filaments based on interfilament electrostatic and hydrophobic interactions. It predicts that the process is limited by an optimal bundle thickness, which is determined by the electric charge of the filaments, the number of hydrophobic residues in the constituent keratin polypeptides, and the extent to which the electrolyte ions are excluded from the bundle interior. We evaluate the kinetics of the bundling process by considering the energy barrier a filament has to overcome for joining a bundle.

**SIGNIFICANCE** We propose that bundle formation by keratin intermediate filaments is driven by generic physical interactions between the filaments rather than linking of filaments by specialized proteins or specific molecular bonds. According to our model, the filament bundling results from the interplay between the interfilament long-range electrostatic repulsion and short-range hydrophobic attraction.

## INTRODUCTION

The cytoskeleton is a complex system of active polymeric networks, spanning the volume of every mammalian cell and performing multiple functions vital for cell physiology (1). The cytoskeleton consists of three subsystems: 1) actin filaments, which serve as a base for the intracellular force-generating machinery involved in processes such as cell attachment to, spreading on, and crawling along extracellular matrices, intracellular membrane trafficking, and establishment of cell-cell contacts (2); 2) microtubules that are involved in mechanical stabilization and expression of surface specialization, cell division, movement of cellular organelles, and intracellular signal transduction (3); and 3) intermediate filaments (IFs), which maintain cellular integrity by providing cells with mechanical resistance and overall stress protection (4–6). Although actin filaments, microtubules, and their networks have been thoroughly

investigated and characterized in structural, biochemical, and biophysical terms as well as in terms of their bundling (7–9), IFs have remained less understood. Revealing the physical factors, which determine the dynamic and structural properties of IFs will help to understand the role of IF networks in cellular functions.

Cytoplasmic IFs are semiflexible biopolymers characterized by an average cross-sectional diameter of ~10 nm and relatively low bending rigidities corresponding to finite persistence lengths varying between a few hundred nanometers and a few microns (for review, see (4)). The protein composition of IFs varies depending on the cell type and cell function (4,10). Yet, all IFs share a common building principle (11). The constituent elongated protein molecules orient parallel to each other through strong coiled-coil interactions to form polar homo- or heterodimers. The dimers interact in an antiparallel fashion, generating nonpolar tetramers, which, in turn, self-organize into 65-nm-long oligomers that are referred to as the unit length filaments (ULFs). The end-to-end intercalation of these ULFs leads to the formation of microns-long IFs with a diameter of ~10 nm (4).

Submitted December 31, 2019, and accepted for publication May 20, 2020.

\*Correspondence: [michk@tauex.tau.ac.il](mailto:michk@tauex.tau.ac.il) or [urbakh@tauex.tau.ac.il](mailto:urbakh@tauex.tau.ac.il)

Editor: Dimitrios Vavylonis.

<https://doi.org/10.1016/j.bpj.2020.05.024>

© 2020 Biophysical Society.

This is an open access article under the CC BY-NC-ND license (<http://creativecommons.org/licenses/by-nc-nd/4.0/>).



In this study, we consider IFs consisting of keratin molecules that we will refer to as keratin intermediate filaments (KIFs). They are typically expressed in epithelial cells (4,12,13). Observations in live cells revealed increased deformability of keratin-deficient epithelial cells (14,15). Precisely how KIF network organization and dynamics contribute to the mechanical properties of epithelial cells is still only poorly understood (16).

Keratin filaments self-assemble into dynamic networks spanning the entire intracellular space (12). The typical network morphology of cultured cells is depicted at left of Fig. 1. Differences in fluorescence intensity correspond to different KIF bundle thicknesses. A gradual increase in bundling is observed from the cell periphery toward the perinuclear region, which is located at the cell center. The images at right of Fig. 1 exemplify how two adjacent motile filament bundles fuse laterally to form a thicker KIF bundle.

Understanding KIF bundling requires, in the first place, identification of the interfilament interactions driving filament association. Based on that, it has to be determined whether the process proceeds unlimitedly thereby generating indefinitely thick bundles or is, alternatively, restricted by intrinsic factors leading to formation of bundles of a particular thickness. In the latter case, the dependence of the preferred bundle thickness on the interaction parameters has to be revealed.

The forces driving filament bundling can result either from interfilament connections through specific molecular linkers or from generic physical interactions. The latter may involve long-range electrostatic and Van-der Waals forces and short-range effective interactions mediated by

local structuring of water near the filaments such as hydrophobic interactions (17). The short-range attractive forces between the filaments can include also the interactions mediated by the charge fluctuation and correlation effects in the presence of multivalent counterions (for a review, see (18)).

Filaggrin has been proposed to be a specific molecular linker (19,20). It has been shown that Filaggrin binds to keratin 1 and 10 filaments as well as other types of KIFs resulting in tight IF bundles (19,20). Yet, cell collapsing and flattening, which had been suggested to be facilitated by the Filaggrin-mediated KIF bundling, occur also in the absence of Filaggrin (19). This observation questions the necessity of Filaggrin for KIF bundle formation and suggests that generic interactions play the major role in KIF bundling. Indeed, generation of K8/K18 bundles by generic interactions between KIFs was demonstrated in experiments in which the keratin molecules were added to aqueous solutions of salt in the absence of any other agents (21). The onset of the bundling process was substantially affected by salt concentration and pH level, whose optimal values corresponded to the physiological conditions in the cytoplasm (21). The effects of the concentrations and valences of the ions in the electrolyte solutions were addressed in detail for bundling of vimentin filaments (22,23), which, despite different molecular charge and hydrophobicity, is expected to be driven by the same interactions as bundling of K8/K18 filaments (24).

Here, we focus on the mechanism of KIF bundle formation, mostly using the data obtained for KIFs consisting of keratin 8 and keratin 18. The strong dependence of the bundling process on the pH and salt concentration indicates that one of the involved interfilament interactions must be the electrostatic repulsion because of the substantial overall electric charge of K8/K18 filaments at physiological pH (21). To overcome the repulsion and drive filament association, a strong attractive interaction must act between the filaments. A feasible candidate for such interaction is the effective short-range attraction between the hydrophobic residues of the central rod and tail domains of the filaments. Such hydrophobic residues are abundant in K8/K18 and their interaction has been proposed to be responsible for the high elastic moduli and the strain-stiffening of K8/K18 networks (25).

Here, we consider the physical mechanisms behind the generation of KIF bundles from single filaments. We consider the bundling process to be driven by the interplay between the long-range interfilament electrostatic repulsion and the effective short-range hydrophobic attraction. We predict the existence of an optimal cross-sectional radius of KIF bundles and analyze its dependence on the filament charge and the degree of hydrophobicity. We further evaluate the kinetics of KIF bundle formation by considering the energy barrier for filament merging a bundle and estimating the characteristic time of this event.

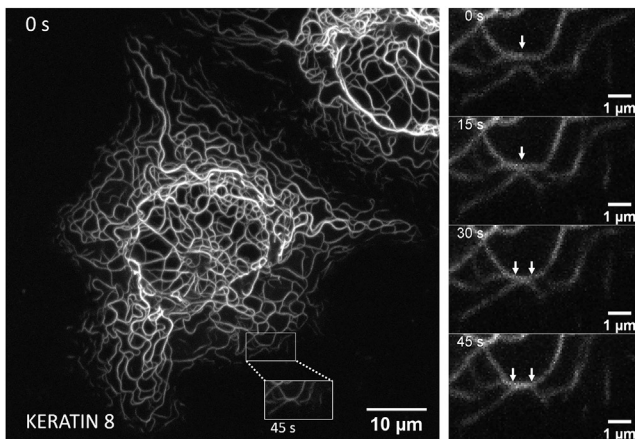


FIGURE 1 Fluorescence microscopy image of keratin 8 in living cells. The keratin 8/18 intermediate filament network is delineated in the cytoplasm of two adjacent adrenal-cortex-derived SW13 cells synthesizing fluorescently labeled keratins 8 and 18 (31). The pictures show the maximum intensity projections of seven focal planes that were imaged every 15 s using a confocal-laser-scanning microscope (LSM710 with an Airyscan detector; Carl Zeiss, Oberkochen, Germany). Bundling of KIFs is observed within the network as illustrated in the inserted time window and the selected time points in the enlarged images at right (arrows demarcate a fusion event).

## METHODS

### Model

Our goal is to analyze the bundling of KIFs by evaluating the radii of the resulting filament bundles and by assessing the time rates for a filament to join a bundle, which set the kinetics of the process.

### Description of the system

We consider a bundle to consist of straight filaments, packed side by side parallel to each other, such that the filament cross sections form a two-dimensional hexagonal lattice (Fig. 2, A and B). We assume the bundle to have a circular cross section with radius  $R$ , denote the cross-sectional radius of a single filament by  $r_f$ , and the shortest distance between the filament surfaces within the bundle by  $2l$  (Fig. 2, A and B). The half edge-to-edge distance  $l$  between nearest neighbors was measured experimentally (26) as  $\sim 2$  nm. The number of filaments,  $N_f$ , within the bundle can be approximately related to the geometrical characteristics of the bundle by

$$N_f \approx \frac{R^2}{(r_f + l)^2} \quad (1)$$

We assume the bundling process to be governed by the interplay between the interfilament electrostatic repulsion and short-range hydrophobic attraction, which determine the bundling energy,  $F_B$ , whose meaning is the thermodynamic work performed in the course of bundle formation out of the, initially, infinitely separated and, therefore, noninteracting filaments. The bundling energy,  $F_B$ , is a sum of the electrostatic,  $F_E$ , and hydrophobic,  $F_H$ , contributions,  $F_B = F_H + F_E$ , where all energies are related to the unit length of the bundle. Our goals are 1) to analyze the dependency of  $F_B$  on the number of filaments,  $N_f$ , within the bundle; 2) to find the conditions in which the bundling energy is negative,  $F_B < 0$ , meaning that the bundling process is energetically favorable; 3) and to determine the optimal number of filaments within the bundle,  $N_f^*$ , corresponding to a minimum of the energy,  $F_B$ .

To evaluate the kinetics of bundling, we use the transition state approach based on determination of the energy barrier a filament has to overcome for joining the bundle. The energy barrier results from the interplay of two factors. First is the energy of the electrostatic repulsion between the filament and the bundle. Second is the elastic bending energy of curved configuration (Fig. 2 C) the filament has to adopt before the

short-range hydrophobic attraction takes over and completes the filament merging with the bundle (Fig. 2 D).

### Interaction energies

We attribute the hydrophobic energy,  $F_H$ , to the interaction between the hydrophobic amino acids of the ULF building blocks. One K8/K18 ULF consists of eight laterally associated tetramers, each made of two dimers, each dimer including 84 hydrophobic amino acids (25). The hydrophobic energy per such amino acid,  $\epsilon_H$ , whose meaning is the difference between the energy values of the hydrophobic acid in aqueous environment and in the contact with other hydrophobic amino acid, can have values (27) between  $-0.9 k_B T$  and  $-5.7 k_B T$  (where  $k_B T \approx 410^{-21}$  Joule is the thermal energy). Considering the pairwise character of the hydrophobic interaction, its total energy per ULF can vary between  $-570 k_B T$  and  $-3800 k_B T$  so that the energy per unit length of the 65 nm long ULF,  $\epsilon_H$ , is within the range,

$$-60 k_B T / \text{nm} \leq \epsilon_H \leq -9 k_B T / \text{nm}$$

Because the hydrophobic interaction acts between pairs of adjacent filaments, the hydrophobic energy per unit length of a bundle,  $F_H$ , is proportional to the number of filaments,  $N_f$ , and using Eq. 1 it can be presented as

$$F_H = \epsilon_H \frac{R^2}{(r_f + l)^2} \quad (2)$$

The energy of electrostatic repulsion,  $F_E$ , originates from the negative charge carried by KIFs, which, for K8/K18 filaments upon a physiological pH, constitutes about three electron charges per nanometer of the filament length (4). Although the charges belong to the specific residues and are, hence, confined to localized spots on the filament backbone, we will use the approximation of even charge distribution along the filament length, which is described by a homogeneous linear charge density of  $\xi = -3e/\text{nm}$  (where  $e = -1.610^{-19}$  C is the electron charge).

We consider the bundle to be immersed into an aqueous electrolyte solution characterized by the dielectric constant  $\epsilon_s \approx 80$  and the screening length (Debye length)  $\lambda$ , which, for the case of a 1:1 electrolyte, is related to the electrolyte concentration  $c_e$ , the electron charge  $e$ , and the electric constant  $\epsilon_0$ , by  $\lambda = \sqrt{(\epsilon_s \epsilon_0 k_B T / e^2 c_e)}$  and constitutes about  $\lambda \approx 1$  nm for physiological electrolyte concentrations of  $c_e \approx 100$  mM. Despite a fairly dense packing of filaments within a bundle (11,26), the electrolyte solution should be able to penetrate the space remaining between the filaments to an unknown extent.

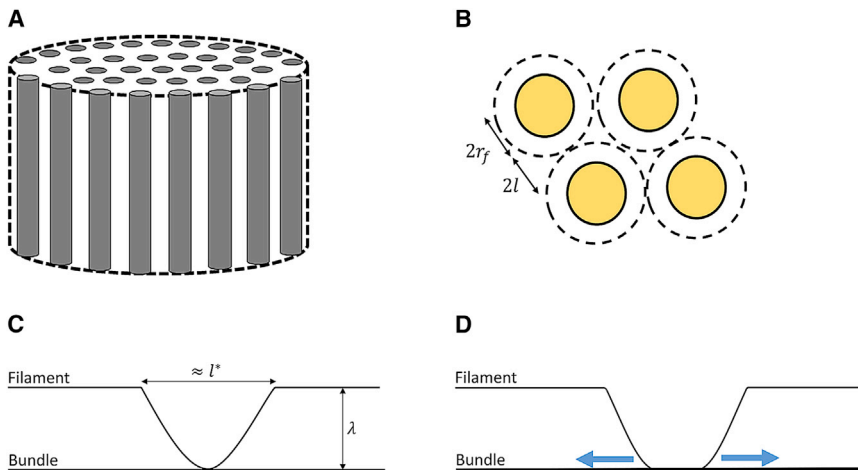


FIGURE 2 Illustration of the model. (A) Cartoon illustrating the close packing of K8/K18 filaments in a bundle. (B) Cartoon showing a fragment of a bundle cross section. The cross-sectional diameter of a filament is  $2r_f$ , and the half-edge-to-edge distance between neighboring filaments is  $2l$ . (C) Creation of a bulge on the filament mediating a point contact between the filament and the bundle, illustrating the critical transition state. (D) Illustration of the zippering process downstream the point contact formation. To see this figure in color, go online.

To proceed, we use a major simplification by neglecting the unknown microscopic details of the distribution within the bundle of the filament charges and the electrolyte ions. Instead, we use the “smeared” approximation considering the intrabundle space as a homogeneous medium. Specifically, we disregard the fact that the charges are located in specific discrete spots on filaments separated by certain distances. We consider the charges as being evenly smeared over the whole internal volume of the bundle  $V^B$ , which includes the overall volume occupied by the filaments  $V^F$  and that of the interfilament space  $V^{int}$ . The resulting volume charge density within the filament,  $\rho_{eff}$ , is regarded to be homogeneous and equal to the total KIF charge within the bundle,  $Q^F$ , divided by the total volume of the bundle,  $\rho_{eff} = Q^F/V^B$ .

A similar approximation is used for the distribution of the electrolyte ions, which penetrate the bundle and are, in reality, localized only to the gaps between the filaments. We consider the total number of the electrolyte ions within the bundle,  $N^B$ , to be evenly distributed over the intrabundle volume,  $V^B$ , which includes the volume occupied by the filaments,  $V^F$ , and that of the gaps between the filaments,  $V^{int}$ . The effective concentration of the electrolyte ions inside the bundle,  $c_{eff}$ , is assumed to be homogeneous and equal to  $c_{eff} = N^B/V^B$ . Because a large part of the intrabundle volume  $V^B$  is, according to electron micrographs (28), occupied by the filaments, the total number of ions within the bundle  $N^B$  is relatively small so that the effective ion concentration must be smaller than the bulk concentration,  $c_{eff} < c_e$ . This implies that the effective screening (Debye) length of the electrolyte within the bundle,  $\lambda_{eff} \sim 1/\sqrt{c_{eff}}$ , will be larger than that outside the bundle,  $\lambda \sim 1/\sqrt{c_e}$ , so that  $\lambda_{eff} > \lambda$ . To account for the difference between,  $\lambda_{eff}$  and  $\lambda$ , we introduce a parameter  $\alpha$ , which can adopt values between 0 and 1, such that

$$\lambda_{eff} = \frac{\lambda}{(1 - \alpha)} \quad (3)$$

The parameter  $\alpha$ , which can be seen as a measure for the overall electrolyte amount within the bundle, will be referred below to as the electrolyte exclusion parameter. According to Eq. 3, larger values of  $\alpha$  correspond to larger intrabundle effective screening length  $\lambda_{eff}$  and, hence smaller average concentration of electrolyte within the bundle. This parameter cannot be measured directly; however, it can be evaluated indirectly by measuring the force exerted on a filament by a parallel bundle in a force microscopy experiment. This force is predicted to critically depend on the exclusion parameter  $\alpha$  (see Eqs. SB4 and SB10). Finally, the dielectric constant within the bundle will be assumed to have an effective value  $\epsilon_{eff}$  averaged over the bundle volume.

We consider the electrostatic energy of bundling,  $F_E$ , as a thermodynamic work needed to be performed to bring the filament charges from the electrolyte bulk to their positions within the bundle, i.e., the work of charging the bundle (for the method, see (29)). Using the radial symmetry of the bundle and the above-mentioned smeared approximation for the structure of the bundle interior, the process of the bundle charging can be presented as a sequence of intermediate steps each consisting in moving an infinitesimally thin layer of charged volume,  $2\pi R' dR'$ , from the infinity in the surrounding electrolyte solution to the surface of the already charged cylindrical volume of the external radius  $R'$ . The charging process begins with  $R' = 0$  and ends when  $R'$  reaches the external radius of the bundle,  $R$ . The overall electrostatic energy,  $F_E$ , per unit length of the bundle corresponding to this procedure is given by the integral

$$F_E = 2\pi\rho_{eff} \int_0^R \Psi(R') R' dR', \quad (4)$$

where  $\Psi(R')$  is the electric potential on the surface of the intermediate charged cylinder with the radius,  $R'$ , determined with respect to the point in the bulk solution infinitely remote from the cylinder.

## Kinetics of bundling

Within the transition state approach, the kinetics of bundling are set by the energy barrier,  $F^*$ , that a filament has to overcome as it approaches and joins the bundle. The characteristic time of the bundling reaction,  $t$ , is given by

$$t = \tau \exp\left(\frac{F^*}{k_B T}\right), \quad (5)$$

where the pre-exponential factor  $\tau$  is the intrinsic time constant of the system, and  $k_B T$  is the thermal energy. To determine  $F^*$  and  $\tau$ , we have to define the transition configuration of the filament-bundle system, which has to be reached for the attractive hydrophobic forces to take over and drive the filament merging with the bundle. Although there may be multiple configurations of this kind, the reaction must, preferably, proceed via the one whose energy is smaller than those of the other transition configurations, and which will be referred below to as the critical transition configuration. The energy of the critical transition configuration represents the energy barrier,  $F^*$ , of the process.

The possibility for the system to adopt various configurations is due to the filament and bundle curvature flexibility, which enables their bending deformations in the course of the mutual approaching. We will assume the bundle to be considerably thicker and, consequently, much stiffer than the filament such that the bundle remains straight, whereas the filament can undergo bending.

The filament bending enables configurations in which only a small fraction of the filament gets close to the bundle, whereas most of the filament length remains remote from it (Fig. 2 C). In such configurations, the filament, while storing some energy of bending, accumulates a comparatively low amount of the energy of electrostatic repulsion. Reaching a configuration in which the local filament-bundle contact is sufficiently tight to allow the hydrophobic attraction to overcome the electrostatic repulsion must be sufficient for starting the process of the filament-bundle merging. Indeed, downstream of such configuration, referred to below as the tight-local-contact configuration, the merging of the filament with the bundle can proceed by simple “zippering” (Fig. 2 D), which guarantees a continuous decrease of the overall system energy. Hence, the critical transition configuration must be a tight-local-contact configuration.

To define the critical transition configuration, we assume that the filament is transported toward the bundle by weak forces generated by cytoplasmic machinery such as cytoskeleton-associated molecular motors. As a result, the filament is aligned parallel to the bundle such that the distance between the filament and the bundle equals the electrostatic screening length  $\lambda$ , which implies that further approaching of the filament to the bundle is stopped by the electrostatic repulsion. The remaining distance,  $\lambda$ , must be bridged by bulging of a section of the filament, which touches the bundle pointwise (Fig. 2 C). The configuration of the filament bulge is set by the interplay between the filament-bundle electrostatic repulsion  $F_E^b$ , which favors narrow bulges, and the bending energy of the filament fragment forming the bulge  $F_B^b$ , which supports wide bulges. Hence, the optimal shape of the bulge has to be found by minimizing the energy sum  $F^b = F_E^b + F_B^b$  and will be characterized by the resulting length of the bulge profile  $l^*$  (Fig. 2 C). As already mentioned, the energy of the optimal bulge represents the energy barrier,  $F^*$ , of the bundling reaction. Because the shape and energy of the optimal bulge profile are set by the interplay between the electrostatic and the bending energy of the bulging section of the filament, both the bulge length  $l^*$  and the energy barrier  $F^*$  strongly depend on the filament bending modulus and effective electric charge. It has to be emphasized that in our model, the bulge is considered to form through a local thermal fluctuation of filament shape rather than the buckling instability.

We determine the intrinsic time constant  $\tau$  (Eq. 5) as the time that would be needed for formation of the critical transition bulge anywhere along the filament in a hypothetical case of a vanishing energy barrier  $F^* = 0$ . For the sake of estimations, we consider, approximately, the bulge formation as the diffusion of an effective particle representing the filament section whose

length equals that of the bulge  $l^*$  to the distance  $\lambda$  separating the filament and the bundle. The diffusion coefficient of the particle,  $D$ , will be estimated using the Einstein formula,  $D = \mu k_B T$ , with the mobility,  $\mu = (2\pi\eta l^*)^{-1} \ln(l^*/r_f)$ , corresponding to the limiting case of a prolate spheroid with principle axes equal to the filament diameter  $2r_f$  and the bulge length  $l^*$  such that the ellipsoid aspect ratio is  $(l^*/2r_f) \gg 1$  (30). The time needed for bulge formation in a specific location along the filament (for  $F^* = 0$ ) can be estimated as  $\tau_1 = (\lambda^2/D)$ . We estimate the characteristic time of bulge formation anywhere along the filament of the total length,  $L$ , as  $\tau = (\tau_1/M)$ , where  $M = (L/l^*)$  is the number of the potential locations. As a result, we estimate the pre-exponential factor in Eq. 5 as

$$\tau = \frac{\lambda^2 l^*}{D L} \quad (6)$$

## RESULTS

### Thickness of the bundle

The derivations and numerical computations, necessary for determination of the electrostatic energy of the bundle are presented in full detail in [Supporting Materials and Methods](#), Section SA. The dependence of the total energy of the bundle,  $F_B = F_H + F_E$ , on the bundle radius,  $R$ , is determined by energy of the hydrophobic attraction between the filaments,  $\epsilon_H$ , and the parameters setting the extent of the interfilament electrostatic repulsion, which are the effective

charge density within the bundle  $\rho_{eff}$ , the electrolyte screening (Debye) length outside the bundle  $\lambda$ , and the electrolyte exclusion parameter  $\alpha$ . The results of a numerical computation of this dependence, based on Eqs. 2 and 4, are presented in Fig. 3, A and B for K8/K18 characteristic parameters, for different values of the parameter  $\alpha$ , and for two limiting values of  $\epsilon_H$ . According to these results, there are different regimes of bundling depending on the values of  $\epsilon_H$  and  $\alpha$ .

For a low-enough  $\alpha$  and a high-enough  $\epsilon_H$ , the bundling energy is predicted to monotonously decrease for all values of  $R$ . The reason is that under these conditions, the electrostatic interaction between the filaments is strongly weakened by the electrolyte ions, which efficiently penetrate the bundle and, according to Eq. 3, reduce the effective screening length within the bundle  $\lambda_{eff}$  to the values similar to those in the surrounding solution. As a result, the strong hydrophobic attraction between the filaments overcomes the electrostatic repulsion independently of the bundle cross-sectional radius,  $R$ , which results in a decrease of the total energy over the whole range of  $R$ . This predicts unrestricted bundling without limitation of the bundle thickness.

In the limiting case of  $\alpha$  being sufficiently close to 1 and small values of the hydrophobic energy  $\epsilon_H$ , the total energy monotonously increases with the bundle cross-sectional radius

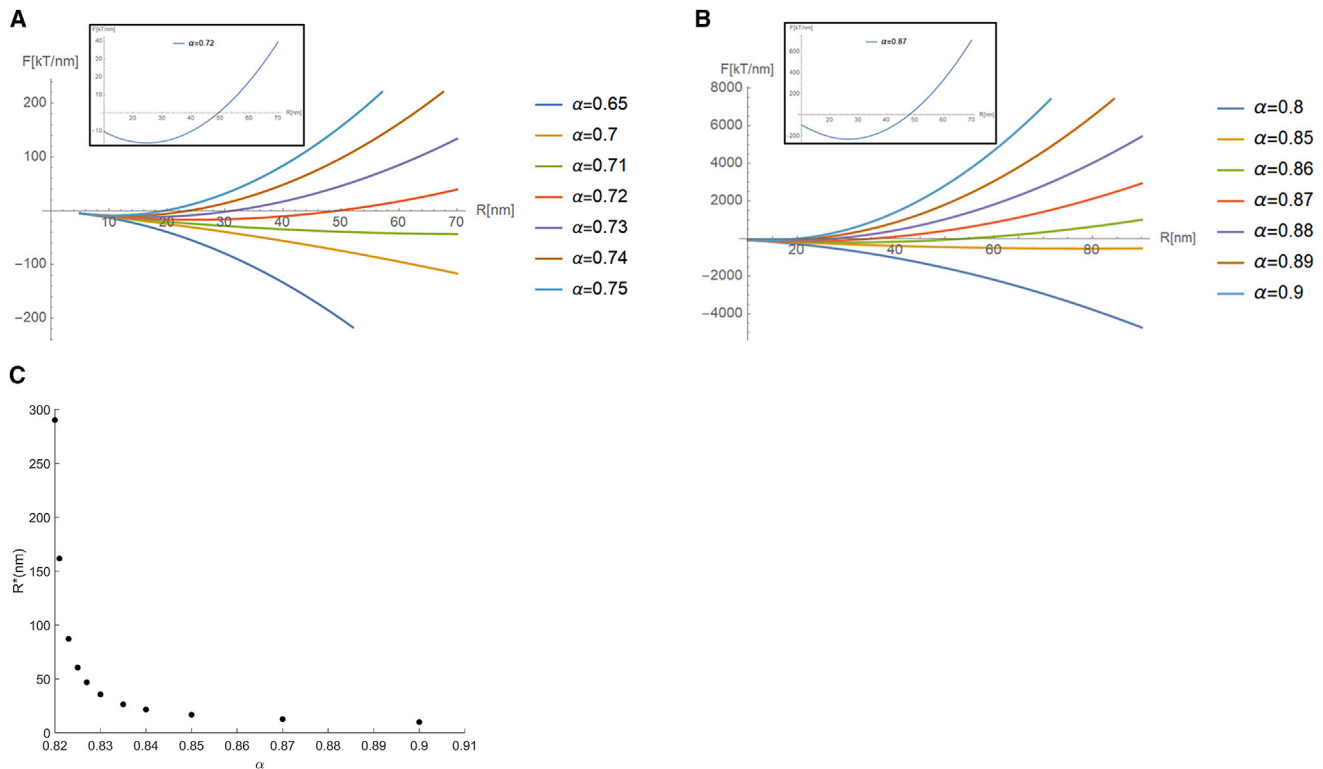


FIGURE 3 Analysis of optimal bundle configuration, a state of minimal bundle energy. (A and B) The bundle energy profile as a function of the cross-sectional radius for different values of  $\alpha$ . The effective intrabundle charge density,  $\rho_{eff} = 3.12 \times 10^{-21}$  (C/nm<sup>3</sup>), corresponds to K8K18 filaments,  $\lambda = 1$  nm and the energy of hydrophobic attraction is (A)  $\epsilon_H = -8.78$  k<sub>B</sub>T/nm and (B)  $\epsilon_H = -58.81$  k<sub>B</sub>T/nm. (C) Optimal radius of a bundle's cross section, as a function of the exclusion parameter  $\alpha$ , for the case of  $\rho_{eff} = 3.12 \times 10^{-21}$  (v/nm<sup>3</sup>),  $\lambda = 1$  nm, and a midranged value of the hydrophobic energy,  $\epsilon_H = -33.79$  (k<sub>B</sub>T/nm).

$R$ , which means that filaments are predicted to not form bundles of any thickness. In this situation, the electrostatic repulsion overcomes the relatively small hydrophobic attraction for any interfilament distance, which prevents bundling.

Finally, for the intermediate values of  $\alpha$  and  $\epsilon_H$ , the total energy changes nonmonotonously with the bundle cross-sectional radius  $R$ , having a minimum at a certain radius,  $R^*$ , which corresponds to formation of bundles with finite equilibrium thicknesses. In this case, the effective screening length within the bundle  $\lambda_{eff}$  is large enough so that the electrostatic repulsion between the filaments extends beyond the nearest-neighbor interaction and its energy increases super-linearly with the number  $N_f$  of filaments within the bundle, which is related to the bundle radius by Eq. 1. Yet the short-range hydrophobic attraction retains the nearest-neighbor character with the energy depending linearly on  $N_f$ . As a result, the hydrophobic attraction prevails in the beginning of the bundling process characterized by small filament numbers  $N_f$ , and thus the relatively small cross-sectional radii of the bundle,  $R$ . For larger values of  $N_f$  and  $R$ , the electrostatic repulsion takes over and stops the bundling process.

The different regimes of bundling as determined by the parameters  $\alpha$  and  $\epsilon_H$  are presented as a phase diagram in Fig. 4 A. Within the region of the phase diagram corresponding to the limited bundling, the value for the equilibrium bundle radius  $R^*$  depends on both  $\alpha$  and  $\epsilon_H$ . These values are presented in Fig. 3 C in dependence on  $\alpha$  for an intermediate value of  $\epsilon_H$ .

The analysis of the bundling regimes was also performed for different values of the effective charge density within the bundle  $\rho_{eff}$  and of the screening length  $\lambda$ . The resulting phase diagrams are presented in Fig. 4, B and C.

As expected, according to these phase diagrams, an increase in the parameter  $\alpha$ , determining the electrolyte exclusion from the bundle (Fig. 4 A), and/or an increase of the screening length (Debye length) (Fig. 4 B)  $\lambda$ , and/or increase of  $\rho_{eff}$  (Fig. 4 C) impede the bundling by strengthening of the electrostatic repulsion between the bundle and the filament. For the same reason, the cross-sectional radius of the bundle is expected to decrease as the exclusion parameter  $\alpha$  in-

creases (Fig. 3 C). In contrast, an increase in  $\epsilon_H$ , the hydrophobic attraction energy, will facilitate bundling according to Fig. 4, A–C.

## Rate of bundling

The configuration and energy of the bulge corresponding to the critical transition state of the filament-bundle system is analyzed in Supporting Materials and Methods, Section B and the computed shape of the bulge is presented in Fig. S2 B. The length,  $l^*$ , of the bulge in the critical transition state, whose computed shape is shown in the Fig. S2 B. The bulging length  $l^*$  estimated for the electrostatic screening length  $\lambda = 1$  nm, characterizing the physiological ionic solutions and the filament-bending rigidity (4),  $\kappa_f = 650$  nm  $k_B T$ , is about 60 nm. Hence,  $l^*$  is much smaller than the typical filament length,  $L \sim 1$   $\mu$ m, hence providing a large number,  $M$ , of the potential sites of the bulge formation.

The intrinsic time constant of the system,  $\tau$  (Eq. 6), which serves as a pre-exponential factor in the expression for the rate of the transition state generation (Eq. 5), is presented in Fig. 5 A as a function of the parameter  $\alpha$  characterizing the degree of electrolyte exclusion from the bundle interior. The value of  $\tau$  is expected to be different for diverse types of IFs because of the differences in the filament bending rigidity  $\kappa_f$  and charge, the latter directly related to the charge density in the bundle  $\rho_{eff}$ . The dependences of  $\tau$  on these parameters are presented in Fig. 5 B and in Fig. 5 C. As expected,  $\tau$  increases with increasing bending modulus rigidity (Fig. 5 C). Indeed, larger values of  $\kappa_f$  raise the energy cost of the bulge curvature, and, hence, promote shallower bulge shapes corresponding to larger bulge lengths  $l^*$ , hence, larger  $\tau$ . Increase of the charge density  $\rho_{eff}$  results in decrease of  $\tau$  (Fig. 5 B), which is a consequence of shortening of the bulge length because of a tendency to reduce the region of a tight apposition between the filament and the bundle and to minimize the electrostatic repulsion energy in this way.

The bulge energy representing the energy barrier  $F^*$  of the reaction of filament merging with the bundle is presented in

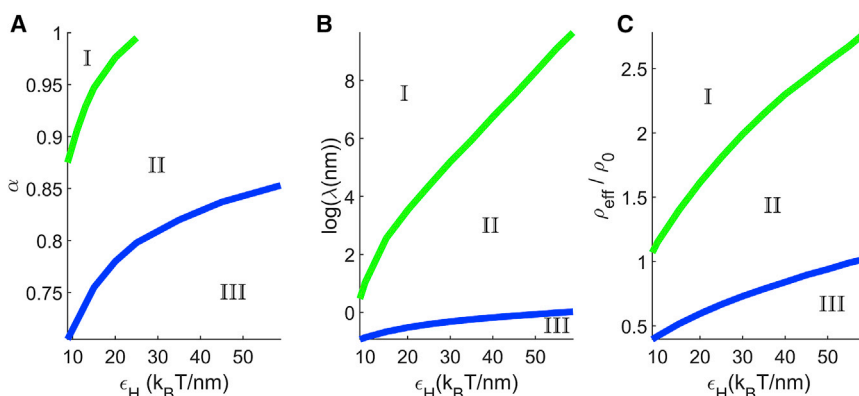


FIGURE 4 Phase diagrams for bundling. Region I shows that no bundling possible. Region II: shows the formation of bundles with a finite equilibrium thickness. Region III shows unlimited bundling. (A) Variation of the exclusion parameter  $\alpha$  and the hydrophobic attraction energy  $\epsilon_H$  for  $\lambda = 1$  nm and the effective charge density  $\rho_{eff} = 3.12 \times 10^{-21}$  C/nm<sup>3</sup> typical for bundles of K8/K18 filaments. (B) Variations of the screening (Debye) length  $\lambda$  and the hydrophobic attraction energy  $\epsilon_H$  for  $\alpha = 0.85$  and the charge density like in (A). (C) Variations of the effective charge density of the bundle,  $\rho_{eff}$ , related to  $\rho_0 = 3.12 \times 10^{-21}$  C/nm<sup>3</sup> for  $\lambda = 1$  nm and  $\alpha = 0.85$ . To see this figure in color, go online.

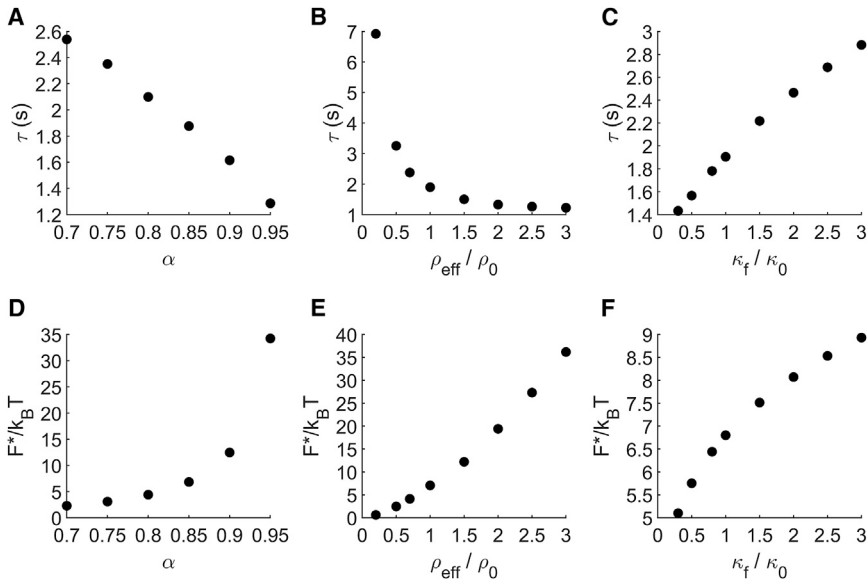


FIGURE 5 The intrinsic time constant in the case of a bundle of a 100-nm diameter and the energy barrier for filament merger to a bundle of a 100-nm diameter calculated as a function of (A and D) the electrolyte exclusion parameter  $\alpha$  for  $\rho_{\text{eff}} = 3.12 \times 10^{-21} \text{ (C/nm}^3\text{)}$ ,  $\kappa_f = 650 \text{ nm k}_B\text{T}$ , and  $\lambda = 1 \text{ nm}$ ; (B and E) the effective charge density in the bundle  $\rho_{\text{eff}}$  related to the K8/K18 charge density  $\rho_0 = 3.12 \times 10^{-21} \text{ (C/nm}^3\text{)}$  for  $\alpha = 0.85$ ,  $\kappa_f = 650 \text{ nm k}_B\text{T}$ , and  $\lambda = 1 \text{ nm}$ ; and (C and F) the filament-bending rigidity  $\kappa_f$ , related to the K8/K18 filament-bending rigidity  $\kappa_0 = 650 \text{ nm k}_B\text{T}$ , for  $\alpha = 0.85$ ,  $\rho_{\text{eff}} = 3.12 \times 10^{-21} \text{ (C/nm}^3\text{)}$ , and  $\lambda = 1 \text{ nm}$ .

Fig. 5, D–F as a function of the system’s various parameters. A strong dependence of  $F^*$  on  $\alpha$  (Fig. 5 D) describes the essential contribution of the electrostatic repulsion between the filament and the bundle to the energy barrier. For a given  $\alpha$ , the energy barrier is predicted to increase with the effective charge density (Fig. 5 E) and with the filament-bending rigidity (Fig. 5 F).

The typical time  $t$  of the filament merging with a bundle, obtained from Eqs. 5 and 6 and the numerical results for  $\tau$  and  $F^*$ , are presented in Fig. 6 as functions of the system’s various parameters. The typical time for bundling increases with the Debye length, and/or effective charge density, and/or the exclusion parameter  $\alpha$ . Fluorescence imaging of the KIF networks (Fig. 1) shows that the typical time of zippering is of the order of 10 s (31).

## DISCUSSION

We presented a model for bundle formation by KIFs based on the interplay between the interfilament electrostatic

repulsion and the hydrophobic attraction between the nonpolar residues of the keratin molecules. The repulsion strength is determined by the effective charge density of the bundle  $\rho_{\text{eff}}$ , the electrolyte screening length outside the bundle  $\lambda$ , and the parameter  $\alpha$ , determining the extent of the electrolyte exclusion from the bundle. The attraction is quantified by the linear hydrophobic energy of a filament,  $\epsilon_H$ .

The model predicted that, depending on the parameters, the filaments undergo different regimes of bundling. If the electrostatic repulsion is strong compared to the hydrophobic attraction, which happens for relatively large charge densities  $\rho_{\text{eff}}$ , and/or large screening length  $\lambda$ , and/or large electrolyte exclusion parameter  $\alpha$ , the filaments are predicted not to undergo bundling. In the opposite case of a relatively strong attraction corresponding to the large hydrophobic energy parameter  $\epsilon_H$ , the filaments are predicted to undergo assembly into unlimitedly thick bundles. Finally, for mutually comparable strengths of the two competing interactions, the model predicted formation of bundles of

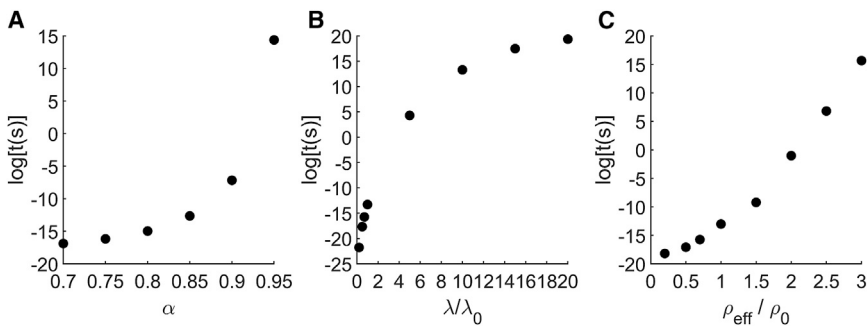


FIGURE 6 Semilogarithm presentation of the characteristic time of bundling reaction for a filament of length  $1 \mu\text{m}$ , and bending rigidity  $\kappa_f = 650 \text{ nm k}_B\text{T}$ , as a function of (A) the electrolyte exclusion parameter  $\alpha$  for an effective charge density  $\rho_{\text{eff}} = 3.12 \times 10^{-21} \text{ (C/nm}^3\text{)}$  and a screening (Debye) length  $\lambda = 1 \text{ nm}$ . (B) The screening (Debye) length  $\lambda$ , relative to its typical value of  $\lambda_0 = 1 \text{ nm}$  for an effective charge density  $\rho_{\text{eff}} = 3.12 \times 10^{-21} \text{ (C/nm}^3\text{)}$ , and an electrolyte exclusion factor  $\alpha = 0.85$ . (C) The effective charge density  $\rho_{\text{eff}}$ , relative to its typical value  $\rho_0 = 3.12 \times 10^{-21} \text{ (C/nm}^3\text{)}$ , for an electrolyte exclusion factor  $\alpha = 0.85$  and an electrolyte screening (Debye) length  $\lambda = 1 \text{ nm}$ .

finite thicknesses whose values depend on the relationship between the parameters  $\rho_{eff}$ ,  $\lambda$ , and  $\alpha$  on one hand and  $\epsilon_H$  on the other. The qualitative reason for the existence of the finite bundle thicknesses is the scale difference between the relatively long-range electrostatic and the short-range hydrophobic interactions.

The model predictions concerning the bundling extent, which are quantitatively illustrated by the phase diagrams (Fig. 4, A–C), agree with the qualitative observations reported in the literature. Based on comparison of the relative filament charges and the degrees of hydrophobicity for three types of intermediate filaments—K8/K18, Vimentin, and Desmin filaments—it has been suggested that a comparatively low negative charge combined with a high relative hydrophobicity will promote bundling of the filaments at a lower concentration and valences of ions (24). This conclusion agrees with the phase diagrams (Fig. 4, B and C). According to the diagram (Fig. 4 B), the higher the filament hydrophobicity expressed through  $\epsilon_H$ , the larger values of the electrolyte screening length  $\lambda$ , and, hence, the smaller electrolyte concentration and valencies enable the bundling onset, as indicated by the corresponding boundary line. The diagram presented in Fig. 4 C predicts that the higher the filament charge accounted by  $\rho_{eff}$ , the higher degree of hydrophobicity  $\epsilon_H$  is needed for bundling to occur.

Comparison of the computed values of the cross-sectional bundle radii with those observed in experiments enables estimation of the electrolyte exclusion parameter  $\alpha$ , which is inaccessible to a direct experimental determination.

The thicknesses of KIF bundles in live cells were measured using transmission electron microscopy (28). The results showed a large variability of bundle diameters, ranging between 40 and 130 nm. Considering the dynamic nature of KIF networks in cells (Fig. 1; (12)), it is reasonable to assume that these measurements largely characterized KIF bundles at the transitional rather than final stages of their formation, leaving open the question about the existence of a finite equilibrium thickness of bundles. Evaluation of the equilibrium parameters of KIF bundles was performed in artificial experimental conditions in which keratin 8 and keratin 18 monomers self-assembled in salt solutions rather than in the cytosol and, hence, were not exposed to the physiological intracellular conditions (21). These experiments demonstrated that bundles exhibit a finite equilibrium thickness of  $\sim 100$  nm, which is in partial agreement with *in vivo* data (28). According to our model's results, 100-nm-thick bundles are expected to form if the hydrophobic energy density is about  $\epsilon_H = -34k_B T/\text{nm}$  corresponding to midrange of its feasible values (Fig. 3 C) and the electrolyte exclusion parameter of about  $\alpha = 0.825$ , which means that the electrolyte entering into the bundle is considerably hindered but not completely prevented.

In addition to the outcome of the bundling process, the model enables estimations of the bundling rates in depen-

dence on the parameters of the interfilament interactions. In the course of bundling, the newly joining filaments have to establish a close contact to facilitate the interfilament hydrophobic attraction taking control of and completing the reaction. During this process, the filaments are mutually repelled by the electrostatic forces. This creates an energy barrier of the reaction, which sets the rate of the bundling reaction. As expected, the predicted bundling rate increases upon weakening of the interfilament electrostatic repulsion, which can result from either a decrease of the filament charge density  $\rho_{eff}$ , a decrease of the electrolyte exclusion parameter  $\alpha$ , or a decrease of the electrolyte screening (Debye) length in the outside solution  $\lambda$  resulting from a decrease of the electrolyte concentration (Fig. 6). These predictions are in line with the measurements (21) of the assembly rates of KIFs for different electrolyte concentrations  $c_e$ , showing that, indeed, the increase of  $c_e$  speeds up the filament assembly.

Evaluation of the typical rate of bundling enables an independent estimation of the electrolyte exclusion parameter,  $\alpha$ . According to the observations, the K8/K18 filament bundles form within minutes (12). We estimated the characteristic time of bundling by computing the energy barrier of the reaction (Fig. 5, D–F) and assessing the intrinsic time constant of the system. According to our results, the experimentally relevant time of the K8/K18 bundle formation of about 100 s corresponds to the value  $\alpha = 0.93$  of the electrolyte exclusion parameter. This reasonably agrees with the above estimation of the  $\alpha$  parameter based on the typical value of the cross-sectional radius of K8/K18 bundles, hence, supports the self-consistency of our analysis.

Our analysis is based on the essential assumption that the short-range interfilament attraction leading to bundling originates from the hydrophobic attraction between the nonpolar residues. Attractive interaction was extensively analyzed for neurofilaments (NFs), which are IF polypeptides typically found in neurons (32). Similar to K8/K18 filaments, NFs undergo bundle formation in aqueous solutions in a salt concentration-dependent fashion (21). Whereas NFs exhibit a long-range electrostatic repulsion resulting from the overall net charge of their surface, filament bundling was proposed to be driven by strong short-range interfilament electrostatic attraction because of alternating discrete electric charges that are distributed along the disordered C-termini of NF subunits (32). According to the suggested model (32), this interaction, referred to as “handshaking,” results from overlap of the carboxytermini of the adjacent NFs in such a way that their discrete opposite charges come into direct contact, providing strong Coulomb attraction (32). Importantly, although the bundling was observed for NFs composed of subunits with sufficiently long side chains, the filaments built of short side-chain subunits demonstrated a bare mutual repulsion and did not exhibit bundle formation (32). This implies that attractive “handshaking” interaction can only drive filament bundling if the number of

side-chain alternating charges and, hence, the side chain lengths are sufficiently large. Similar to NFs, K8/K18 filaments carry a net negative charge and must, therefore, experience long-range mutual repulsion. The attractive interaction responsible for their bundling, however, is likely different from handshaking because the filament side chains appear to be too short to support the bundling reaction. Indeed, truncated NFs with side chains of less than 155 residues failed to undergo bundling (32). The two kinds of side chains of human K8/K18 filaments are even shorter, consisting of 44 and 86 residues, respectively (25). Hence, the only alternative attractive interaction acting between KIFs and capable of driving the filament bundling appears to be short-range interaction such as the hydrophobic force, as assumed in this model.

Finally, it has been experimentally shown that the addition of multivalent ions promotes IF bundling at lower salt concentrations as compared to monovalent salts (22,24). Furthermore, it was demonstrated that the addition of multivalent ions to a network of IFs increased its stiffness (33). Adding multivalent ions promotes bundling by two different effects. First, multivalent ions drastically decrease the electrolyte screening (Debye) length  $\lambda$ , which, for monovalent salts, can be obtained only at much higher electrolyte concentrations. This effect is taken into account by our model through the corresponding changes of  $\lambda$ . Second, multivalent ions can serve as effective cross-linkers between charged surfaces and polymers (18) and, hence, can contribute to the short-range attractive force between the IFs. This effect can be included in our model through a contribution to the effective hydrophobic energy  $\epsilon_H$  making this parameter more negative.

## CONCLUSIONS

In this work, we propose a physical mechanism of bundle formation by KIFs, which is based on the interplay between the intrafilament electrostatic repulsion and the short-range hydrophobic attraction. We predict that the bundling process results in bundles of finite thickness, which depends on the system parameters, namely the amount of the filament electric charge, the number of hydrophobic residues per unit length of the filament, and the degree of electrolyte exclusion from the bundle. We provide estimations of the characteristic time of bundling.

## SUPPORTING MATERIAL

Supporting Material can be found online at <https://doi.org/10.1016/j.bpj.2020.05.024>.

## AUTHOR CONTRIBUTIONS

E.H. performed computations, analyzed the results and wrote the article. R.W. and R.E.L. introduced the subject, provided phenomenological data

and the related figure, discussed the results and evaluated their biological significance, and edited the manuscript. M.U. and M.M.K. formulated the physical model, supervised the computations, discussed the results, and wrote the article.

## ACKNOWLEDGMENTS

The project results from the collaboration of R.R., R.E.L., and M.M.K. within European Union H2020-MSCA-ITN InCeM. M.M.K. is supported by SFB 958 “Scaffolding of Membranes” (Germany) and National Research Foundation Singapore - Israel Science Foundation Research Grant 3292/19. M.U. acknowledges the financial support of the Israel Science Foundation, grant 1141/18.

## REFERENCES

- Albers, K., and E. Fuchs. 1992. The molecular biology of intermediate filament proteins. *Int. Rev. Cytol.* 134:243–279.
- Dominguez, R., and K. C. Holmes. 2011. Actin structure and function. *Annu. Rev. Biophys.* 40:169–186.
- Stephens, R. E., and K. T. Edds. 1976. Microtubules: structure, chemistry, and function. *Physiol. Rev.* 56:709–777.
- Block, J., V. Schroeder, ..., S. Köster. 2015. Physical properties of cytoplasmic intermediate filaments. *Biochim. Biophys. Acta.* 1853:3053–3064.
- Etienne-Manneville, S. 2018. Cytoplasmic intermediate filaments in cell biology. *Annu. Rev. Cell Dev. Biol.* 34:1–28.
- Toivola, D. M., P. Strnad, ..., M. B. Omary. 2010. Intermediate filaments take the heat as stress proteins. *Trends Cell Biol.* 20:79–91.
- Walczak, C. E., and S. L. Shaw. 2010. A MAP for bundling microtubules. *Cell.* 142:364–367.
- Bartles, J. R. 2000. Parallel actin bundles and their multiple actin-bundling proteins. *Curr. Opin. Cell Biol.* 12:72–78.
- Tilney, L. G., P. S. Connelly, ..., G. M. Guild. 1998. Why are two different cross-linkers necessary for actin bundle formation in vivo and what does each cross-link contribute? *J. Cell Biol.* 143:121–133.
- Leube, R. E., and N. Schwarz. 2016. Intermediate filaments. In *Encyclopedia of Cell Biology*. R. A. Bradshaw and P. D. Stahl, eds. Elsevier, pp. 569–578.
- Köster, S., D. A. Weitz, ..., H. Herrmann. 2015. Intermediate filament mechanics in vitro and in the cell: from coiled coils to filaments, fibers and networks. *Curr. Opin. Cell Biol.* 32:82–91.
- Windoffer, R., M. Beil, ..., R. E. Leube. 2011. Cytoskeleton in motion: the dynamics of keratin intermediate filaments in epithelia. *J. Cell Biol.* 194:669–678.
- Yoon, S., and R. E. Leube. 2019. Keratin intermediate filaments: intermediaries of epithelial cell migration. *Essays Biochem.* 63:521–533.
- Seltmann, K., A. W. Fritsch, ..., T. M. Magin. 2013. Keratins significantly contribute to cell stiffness and impact invasive behavior. *Proc. Natl. Acad. Sci. USA.* 110:18507–18512.
- Ramms, L., G. Fabris, ..., B. Hoffmann. 2013. Keratins as the main component for the mechanical integrity of keratinocytes. *Proc. Natl. Acad. Sci. USA.* 110:18513–18518.
- Quinlan, R. A., N. Schwarz, ..., R. E. Leube. 2017. A rim-and-spoke hypothesis to explain the biomechanical roles for cytoplasmic intermediate filament networks. *J. Cell Sci.* 130:3437–3445.
- Israelachvili, J. N. 2011. *Intermolecular and Surface Forces*, Third Edition. Academic Press, Burlington, MA.
- Kanduc, M., A. Naji, and R. Podgornik. 2010. Counterion-mediated weak and strong coupling electrostatic interaction between like-charged cylindrical dielectrics. *J. Chem. Phys.* 132:224703.
- Brown, S. J., and W. H. McLean. 2012. One remarkable molecule: filaggrin. *J. Invest. Dermatol.* 132:751–762.

20. Manabe, M., M. Sanchez, ..., B. A. Dale. 1991. Interaction of filaggrin with keratin filaments during advanced stages of normal human epidermal differentiation and in ichthyosis vulgaris. *Differentiation*. 48:43–50.
21. Kayser, J., H. Grabmayr, ..., A. R. Bausch. 2012. Assembly kinetics determine the structure of keratin networks. *Soft Matter*. 8:8873.
22. Dammann, C., and S. Köster. 2014. Dynamics of counterion-induced attraction between vimentin filaments followed in microfluidic drops. *Lab Chip*. 14:2681–2687.
23. Dammann, C., H. Herrmann, and S. Köster. 2016. Competitive counterion binding regulates the aggregation onset of vimentin intermediate filaments. *Isr. J. Chem.* 56:614–621.
24. Hémonnot, C. Y. J., M. Mauermann, ..., S. Köster. 2015. Assembly of simple epithelial keratin filaments: deciphering the ion dependence in filament organization. *Biomacromolecules*. 16:3313–3321.
25. Pawelzyk, P., N. Mücke, ..., N. Willenbacher. 2014. Attractive interactions among intermediate filaments determine network mechanics in vitro. *PLoS One*. 9:e93194.
26. Hémonnot, C. Y. J., J. Reinhardt, ..., S. Köster. 2016. X-rays reveal the internal structure of keratin bundles in whole cells. *ACS Nano*. 10:3553–3561.
27. Tanford, C. 1980. *The Hydrophobic Effect: Formation of Micelles and Biological Membranes*, Second Edition. J. Wiley, New York.
28. Nolting, J. F., W. Möbius, and S. Köster. 2014. Mechanics of individual keratin bundles in living cells. *Biophys. J.* 107:2693–2699.
29. Verwey, E. J. W. 1947. Theory of the stability of lyophobic colloids. *J. Phys. Colloid Chem.* 51:631–636.
30. Chwang, A. T., and T. Y. Wu. 1976. Hydromechanics of low-Reynolds-number flow. Part 4. Translation of spheroids. *J. Fluid Mech.* 75:677–689.
31. Wöll, S., R. Windoffer, and R. E. Leube. 2005. Dissection of keratin dynamics: different contributions of the actin and microtubule systems. *Eur. J. Cell Biol.* 84:311–328.
32. Beck, R., J. Deek, and C. R. Safinya. 2012. Structures and interactions in ‘bottlebrush’ neurofilaments: the role of charged disordered proteins in forming hydrogel networks. *Biochem. Soc. Trans.* 40:1027–1031.
33. Lin, Y.-C., C. P. Broedersz, ..., D. A. Weitz. 2010. Divalent cations crosslink vimentin intermediate filament tail domains to regulate network mechanics. *J. Mol. Biol.* 399:637–644.